Earth and Planetary Science Letters 507 (2019) 140–153

Contents lists available at ScienceDirect

Earth and Planetary Science Letters

www.elsevier.com/locate/epsl

^{10}Be erosion rates controlled by transient response to normal faulting through incision and landsliding

Duna C. Roda-Boluda [a,*], Mitch D'Arcy [a,1], Alexander C. Whittaker [a], Delia M. Gheorghiu [b], Ángel Rodés [b]

[a] Department of Earth Science & Engineering, Imperial College London, Royal School of Mines, Prince Consort Road, SW7 2BP London, United Kingdom
[b] Scottish Universities Environmental Research Centre (SUERC), Scottish Enterprise Technology Park/Rankine Av, G75 0QF Glasgow, United Kingdom

ARTICLE INFO

Article history:
Received 19 February 2018
Received in revised form 18 November 2018
Accepted 23 November 2018
Available online 13 December 2018
Editor: A. Yin

Keywords:
cosmogenic nuclides
erosion rates
normal faults
incision
landslides
transient response

ABSTRACT

Quantifying erosion rates, and how they compare to rock uplift rates, is fundamental for understanding landscape response to tectonics and associated sediment fluxes from upland areas. The erosional response to uplift is well-represented by river incision and the associated landslide activity. However, characterising the relationship between these processes remains a major challenge in tectonically active areas, in some cases because landslides can preclude obtaining reliable erosion rates from cosmogenic radionuclide (CRN) concentrations. Here, we quantify the control of tectonics and its coupled geomorphic response on the erosion rates of catchments in southern Italy that are experiencing a transient response to normal faulting. We analyse in-situ ^{10}Be concentrations for detrital sediment samples, collected along the strike of faults with excellent tectonic constraints and landslide inventories. We demonstrate that ^{10}Be-derived erosion rates are controlled by fault throw rates and the extent of transient incision and associated landsliding in the catchments. We show that the low-relief sub-catchments above knickpoints erode at uniform background rates of ~0.10 mm/yr, while downstream of knickpoints, erosion removes ~50% of the rock uplifted by the faults, at rates of 0.10–0.64 mm/yr. Despite widespread landsliding, CRN samples provide relatively consistent and accurate erosion rates, most likely because landslides are frequent, small, and shallow, and represent the integrated record of landsliding over several seismic cycles. Consequently, we combine these validated ^{10}Be erosion rates and data from a geomorphological landslide inventory in a published numerical model, to gain further insight into the long-term landslide rates and sediment mixing, highlighting the potential of CRN data to study landslide dynamics.

1. Introduction

The balance between uplift and erosion determines the evolution of topography, regulates the timescale over which bedrock channels adjust to tectonics (Whipple and Tucker, 1999), and may even influence the evolution of active faults (Olive et al., 2014). Therefore, erosion rate data are particularly useful when they can be compared to known rock uplift rates or fault throw rates (Stock et al., 2009; Densmore et al., 2009; Cyr et al., 2010), with which they are expected to scale by a function modulated by lithology, climate, and erosional dynamics.

Mountain ranges bounded by normal faults are ideal settings to study erosional landscape responses to tectonics, because they are typically characterised by strong along-strike uplift gradients, with high fault slip rates at fault centres that decay to zero at the fault tips (e.g. Cowie and Roberts, 2001). This tectonic gradient is frequently reflected in the geomorphology of footwall catchments: greater relief, deeper river incision, and steeper channels and hillslopes are generally found where throw rates are greater, and hence erosion rates are expected to vary accordingly (Densmore et al., 2004; Whittaker et al., 2008; Roda-Boluda and Whittaker, 2017, 2018). This coupling of fault activity and erosion is supported by numerical (Cowie et al., 2006) and analogue (Strak et al., 2011) models of landscape response to normal faulting. However, few empirical studies have tested this explicitly using cosmogenic radionuclides (CRN), and those found little correlation between CRN erosion rates and fault throw rates (Stock et al., 2009;

* Corresponding author. Current address: GFZ German Research Centre for Geosciences, Telegrafenberg, 14473 Potsdam, Germany.
E-mail addresses: roda@gfz-potsdam.de (D.C. Roda-Boluda), mdarcy@uni-potsdam.de (M. D'Arcy), a.whittaker@imperial.ac.uk (A.C. Whittaker), Delia.Gheorghiu@glasgow.ac.uk (D.M. Gheorghiu), Angel.Rodes@glasgow.ac.uk (Á. Rodés).
[1] Current address: University of Potsdam, Institute of Earth and Environmental Science, Karl-Liebknecht-Str. 24-25, 14476 Potsdam Golm, Germany.

https://doi.org/10.1016/j.epsl.2018.11.032
0012-821X/

Densmore et al., 2009, in the Basin and Range). In both studies, the discrepancy was attributed to the role of stochastic landsliding, the possibility that erosion rates may not average over enough earthquake cycles, and/or transient erosional responses.

In extensional settings, transient erosional responses typically emerge when normal fault throw rates increase due to fault growth and linkage (Cowie and Roberts, 2001; Whittaker et al., 2008). Rivers draining footwall catchments respond to the increased tectonic rates by incising and steepening as knickpoints migrate upstream over timescales of $\sim 10^5$–10^6 years, while the areas above knickpoints remain adjusted to the pre-perturbation state (Cowie et al., 2006; Whittaker et al., 2008; Attal et al., 2011; Kirby and Whipple, 2012). Knickpoints – and hence, incision – migrate faster in catchments affected by greater throw rates or where greater throw rate changes have occurred (Whittaker et al., 2008; Attal et al., 2011; Roda-Boluda and Whittaker, 2017, 2018). Fluvial incision leads to hillslope steepening, which increases the rates of hillslope diffusion and erosion. Once the strength-limited bedrock equilibrium angle has been reached, landsliding becomes the dominant erosional process, and erosion rates may only continue to increase through enhanced landslide activity, rather than by further hillslope steepening (Burbank et al., 1996; Larsen and Montgomery, 2012). Enhanced landslide erosion can occur through increases in the frequency of landslide events and/or increased volumes of mobilised sediment in each event (e.g. Larsen et al., 2010; Korup et al., 2012). This change in dominant erosional process from diffusion to landsliding leads to a non-linear dependence of erosion rate on hillslope angles, as reported by CRN studies (Binnie et al., 2007; Ouimet et al., 2009; DiBiase et al., 2010; Tofelde et al., 2018). In such settings, landslide erosion rates are controlled by uplift and incision rates, and the three rates should have comparable magnitudes (Burbank et al., 1996; Densmore et al., 1998; Binnie et al., 2007). Nevertheless, few studies have explicitly quantified the coupling among uplift, incision, landsliding and erosion rates beyond their spatial coincidence (Burbank et al., 1996; Larsen and Montgomery, 2012), partly because landslides can preclude obtaining reliable erosion rates from CRN concentrations.

In rapidly eroding landscapes where CRN decay is negligible, the catchment-averaged CRN concentration in well-mixed detrital sediment derived from uniform hillslope denudation is proportional to the catchment-averaged CRN production rate and inversely proportional to catchment-averaged erosion rate (Lal, 1991; Bierman and Steig, 1996). CRN production rates are greatest at the rock surface, and decay exponentially to 2% of the surface production rate at ~3 m depth in rock (Brown et al., 1995; Dunai, 2010). Hence, material with low CRN concentrations is sourced from deep and/or rapidly eroding sources (Brown et al., 1995; Bierman and Steig, 1996; Tofelde et al., 2018).

Consequently, landslides mobilise material depleted in CRN relative to other erosional processes. High-magnitude, low-frequency landslide events can generate large amounts of CRN-depleted material, which temporarily dilutes CRN concentrations in river sediments, leading to overestimations of long-term erosion rates (Niemi et al., 2005; West et al., 2014). Alternatively, if sediment flux is dominated by large, infrequent landslides, samples collected between large events may underestimate long-term erosion rates (Niemi et al., 2005; Ouimet, 2010). However, if sediment flux is dominated by frequent, small landslides (<2–3 m deep), CRN samples could still be representative of long-term erosion rates, if sediment is well-mixed (Brown et al., 1995; Niemi et al., 2005; Yanites et al., 2009). Because landslides are produced at point sources, they can violate the assumption of uniform denudation that is needed to convert sediment CRN concentrations into catchment-averaged erosion rates (Yanites et al., 2009; West et al., 2014). Numerical models (Niemi et al., 2005; Yanites et al., 2009) suggest that the influence of landslides on the accuracy of CRN-derived erosion rates depends on: (1) the relative contributions of small, shallow and frequent landslides; large, deep and infrequent landslides; and other erosional processes to the long-term sediment flux; and (2) the degree to which sediment from these different sources is proportionally mixed, spatially and temporally. However, these models have never been applied to test the accuracy of CRN-erosion rates in natural landscapes.

Here, we analyse cosmogenic ^{10}Be concentrations in 15 detrital sand samples, collected above and below knickpoints in transiently responding catchments along normal faults in southern Italy, which we combine with 23 ^{10}Be-derived erosion rates recalculated from previous studies in the area (Cyr et al., 2010; Olivetti et al., 2012). These faults have published high-resolution constraints on fault throw rates and landscape response (Roda-Boluda and Whittaker, 2017, 2018), and a geomorphological landslide inventory with information on landslide volumes is available for the area (Roda-Boluda et al., 2018). Taking advantage of these published constraints, we comprehensively test the controls of fault throw rates, transient incisional responses and landslide activity on catchment-averaged erosion rates. Finally, we use the numerical model of Yanites et al. (2009) to evaluate the landslide recurrence intervals and sediment mixing dynamics (degree of mixing and fluvial versus hillslope mixing) that would be needed to yield accurate ^{10}Be-erosion rates.

2. Geological setting

Normal faulting started by the Lower Pleistocene in the Southern Apennines, and in the Middle Pleistocene in Calabria, as a result of back-arc extension (e.g. Patacca et al., 1990). In the Southern Apennines, we sampled catchments draining the Agri normal fault (Fig. 1), which has had a time-averaged, footwall component of fault throw rates of up to 0.5 ± 0.1 mm/yr for the last ~1 Myr, based on detailed throw-rate profiles derived from seismic, geologic throw and electrical tomography data (Roda-Boluda and Whittaker, 2018). In Calabria, we studied catchments bounded by the Crati, Serre, Cittanova and Armo faults (Fig. 1). Based on throw-rate profiles built from the heights and offsets of marine terraces, and a well-constrained fault initiation time of 1.0 ± 0.2 Ma, the time-averaged footwall component of throw rates since ~1 Ma are up to $0.4^{+0.1}_{-0.1}$ mm/yr on the Serre fault, $0.8^{+0.2}_{-0.1}$ mm/yr on the Cittanova fault, and $0.7^{+0.2}_{-0.1}$ mm/yr on the Armo fault (Roda-Boluda and Whittaker, 2017). For the Crati fault, the minimum footwall component of throw is $0.5^{+0.2}_{-0.2}$ mm/yr, based on extrapolating the seismically-imaged hanging-wall throw (Spina et al., 2011; Roda-Boluda and Whittaker, 2017). Using throw rates representative of the last 1 Myr to compare with CRN erosion rates (representative over 10^2–10^3 yr timescales) could be a source of uncertainty in our study. However, estimates of fault throw rates on 10^3 yr timescales are only available for the central-north sector of the Cittanova Fault, derived from five trenches (Galli and Bosi, 2002; Galli and Peronace, 2015), and these studies obtained estimates of 0.44–0.6 mm/yr which are in good agreement with our longer-term estimates. These faults generate earthquakes of magnitudes M 5.5–7.0 with recurrence intervals on each fault of ~0.3–3.2 kyr; overall southern Italy has been affected by about 20 earthquakes over the last 2 kyr, most recently in 1980 in the Southern Apennines and 1908 in Calabria (Valensise and Pantosti, 2001; Galli and Peronace, 2015).

The upland study area has a Mediterranean climate characterised by mean annual temperatures of ~12 °C and mean annual precipitation of 1200–1600 mm. Sampled footwall catchments are dominated by flysch sandstones for the Agri fault, granites for the Crati, Serre and northern Cittanova faults, and gneisses and schists for the southern Cittanova and Armo faults (Fig. 1). Schmidt hammer measurements indicate that the gneisses and schists have the

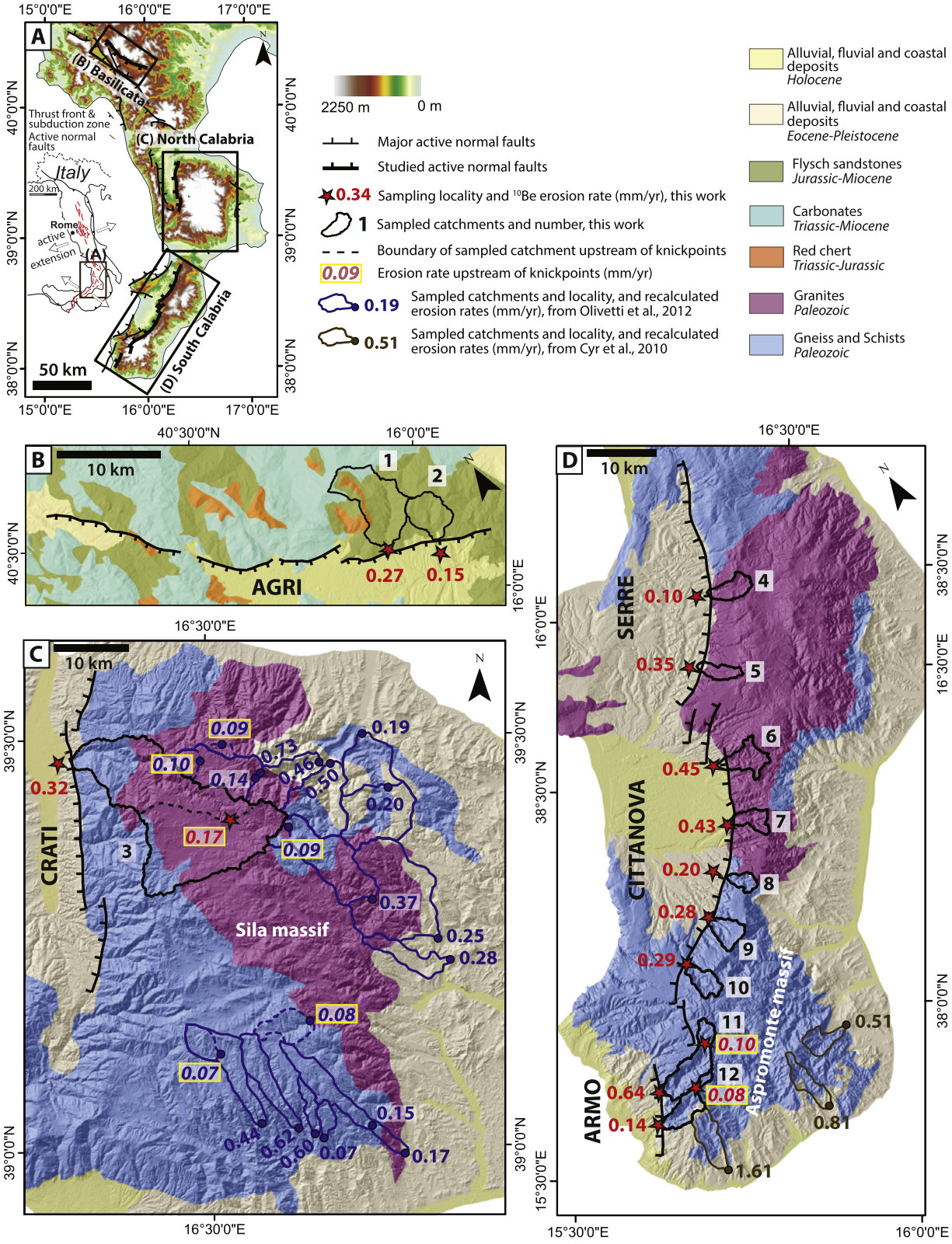

Fig. 1. DEM, fault and lithological maps of the study area, with sampled catchments and ^{10}Be erosion rates. (a) DEM showing the three study areas, with inset showing the geodynamic context. (b) Agri normal fault, Basilicata field area. (c) Crati normal fault and Sila massif, in northern Calabria. (d) Serre, Cittanova and Armo normal faults, and Aspromonte massif, in southern Calabria. Erosion rates from Cyr et al. (2010) and Olivetti et al. (2012) have been recalculated using Cronus v2.3 (see supplementary Table S1). (For interpretation of the colours in the figure(s), the reader is referred to the web version of this article.)

greatest rock strength, with an average rebound value of ∼27, and that flysch and granites have lower average rebound values of ∼17 and ∼21 respectively (Roda-Boluda et al., 2018).

Catchments along the studied faults are transiently responding to an increase in base level lowering rates, evidenced by the presence of knickpoints in the channel long profiles (Fig. 2; cf. Roda-Boluda and Whittaker, 2017, 2018). For the Agri catchments (1 knickpoint, Fig. 2), geomorphic and structural analyses reveal that the transient response was caused by a ∼2–3 fold slip rate acceleration due to fault linkage ∼1 Ma (Roda-Boluda and Whittaker, 2018). The throw rates specified above represent slip rates after this event. For the Calabrian catchments, the highest (or single) set of knickpoints is interpreted to have formed as the faults initiated ∼1 Ma, increasing channel steepness by a factor of ∼2–3. The lower knickpoints, where present, relate to subsequent fault acceleration events that occurred soon after faulting onset in some faults (Roda-Boluda and Whittaker, 2017). Below the knickpoints, catchments are incised and steep; above them, there are less steep channels and hillslopes in some catchments, or unincised remnants of a low-relief landscape in others (Fig. 1 and 2; Olivetti et al., 2012; Roda-Boluda and Whittaker, 2017, 2018). Field observations indicate that there is little fluvial storage in the studied catchments, with low-moderate sediment cover over primarily bedrock channels.

Landslides are common in the studied catchments, generally located along the steep hillslopes of incised valleys below the knickpoints (Fig. 2), and triggered by earthquakes or rainfall (Polemio and Petrucci, 2010). A landslide inventory published by the Italian Geological Survey (IFFI project, e.g. Trigila et al., 2010) has recently been updated with previously unrecognised landslides, with mapped landslide areas between 580 m^2 and 3.7×10^6 m^2 (Roda-Boluda et al., 2018). For this updated inventory of ∼3000 landslides along the studied faults, median-sized landslides are 0.03 km^2, and 85% of mapped landslides are <0.1 km^2, which according to a field-based, local area-volume scaling relationship, corresponds to excavation depths of ∼2.3 m and ∼3 m, respectively (Roda-Boluda et al., 2018; see supplementary information). From this inventory, $\beta = 2.3$ – the dimensionless power-law exponent that defines the decay in frequency of bigger landslides with respect to smaller ones –, indicating that landslide sediment flux is not dominated by large, infrequent landslides (see supplementary material and Roda-Boluda et al., 2018). Multi-temporal studies also indicate that the area is characterised by shallow landsliding, and nine studies report frequencies widely ranging between 1.4×10^{-4} to 3.3×10^0 landslides/yr/km^2 (see supplementary information for a summary table and a full reference list). Landslide densities in the flysch sandstones are twice as large as for other lithologies in the area, suggesting that this lithology is significantly more prone to landsliding (Roda-Boluda et al., 2018).

In Calabria, ^{10}Be erosion rates have been calculated by Cyr et al. (2010), for three catchments draining the SE side of the Aspromonte massif, and by Olivetti et al. (2012), for 20 catchments draining the eastern flank of the Sila massif, including low-relief sub-catchments above knickpoints (Fig. 1). However, these studies did not examine erosion rates in the context of active normal faulting, and the effects of transient incision and coupled landsliding were not explicitly quantified. In the Southern Apennines, estimates of erosion rates range from 0.1–0.5 mm/yr, based on reconstruction of eroded valley volumes (Amato et al., 2003; Lazzari and Schiattarella, 2010; Gioia et al., 2011) and suspended sediment yield (Lazzari and Schiattarella, 2010).

3. Methods

3.1. ^{10} Be sampling and analyses

We collected 15 detrital samples from fluvial bars and active channels, 12 of which were from the outlets of normal fault-bounded footwall catchments, and 3 of which were above knickpoints, at the outlets of the unincised, low relief, upper sub-catchments (Figs. 1 and 2). Catchments were selected to ensure comparison of erosion rates from catchments affected by a range of footwall throw rates and degrees of transient incisional response, and dominated by different lithologies (Table 1; Figs. 1 and 2). The 250–500 μm grain size fraction was used for ^{10}Be analysis, because sand samples are most likely to contain a representative mix of the erosional processes affecting the catchment, and hence, better approximate mean, long-term erosion rates (e.g. Carretier et al., 2015). Samples (10 to 15 g of clean quartz) were prepared and analysed at the SUERC CIAF facility; preparation procedures are detailed in the supplementary information. Catchment-averaged topographic shielding factors and production-rate scalings were calculated from catchment hypsometry using ASTER DEMs for the study area with a horizontal and vertical resolution of 27 m and 1 m, respectively. For each catchment, the elevation that corresponded to its average production-rate scaling value was used for erosion rate calculations, performed with the Cronus v2.3 calculator (Balco et al., 2008); using the input parameters in Table 2. Twenty-three ^{10}Be erosion rates published by Cyr et al. (2010) and Olivetti et al. (2012) are used for comparison, and were recalculated using Cronus v2.3 and the same reference ^{10}Be production rate as our data, which has changed since the original studies were published; input parameters are in the supplementary material.

3.2. Tectonic constraints

We compare erosion rates with the footwall component of fault throw rates (vertical component of slip rates, minus hangingwall sedimentation rates) because this is the vertical uplift rate to which channels draining the footwall adjust (e.g. Whittaker et al., 2008). Each catchment was attributed a throw rate from published throw rate profiles (Roda-Boluda and Whittaker, 2017, 2018) depending on the position of its outlet along strike, as tectonic signals theoretically propagate upstream from this point (e.g. Whittaker et al., 2008). The unincised upper catchments were considered as having effective throw rates of 0 mm/yr, because they still record pre-normal faulting conditions. Fault throw rates have the uncertainty ranges presented in section 2 and in Roda-Boluda and Whittaker (2017, 2018), which arise mostly from uncertainties on fault initiation time and therefore are largely systematic. CRN-derived sediment fluxes were obtained by multiplying ^{10}Be erosion rates by catchment area.

3.3. Geomorphological analyses

Channel long profiles were extracted from the DEM using the Stream Profiler toolbar (Wobus et al., 2006) and slope-break knickpoints (cf. Kirby and Whipple, 2012) bounding a lower section of the channel that registers a ≥10% increase in channel steepness were marked on the long profiles (Fig. 2). Information on the timing and origin of these knickpoints can be found in the Geological Setting; a complete analysis is available in Roda-Boluda and Whittaker (2017, 2018). Time-averaged vertical knickpoint propagation rates for the highest knickpoint in each catchment are estimated as the height of the knickpoint from the fault, divided by the time since that knickpoint was initiated (∼1 Ma). We use maximum incision depth, calculated as the maximum vertical distance between the drainage divide and the valley bottom in each

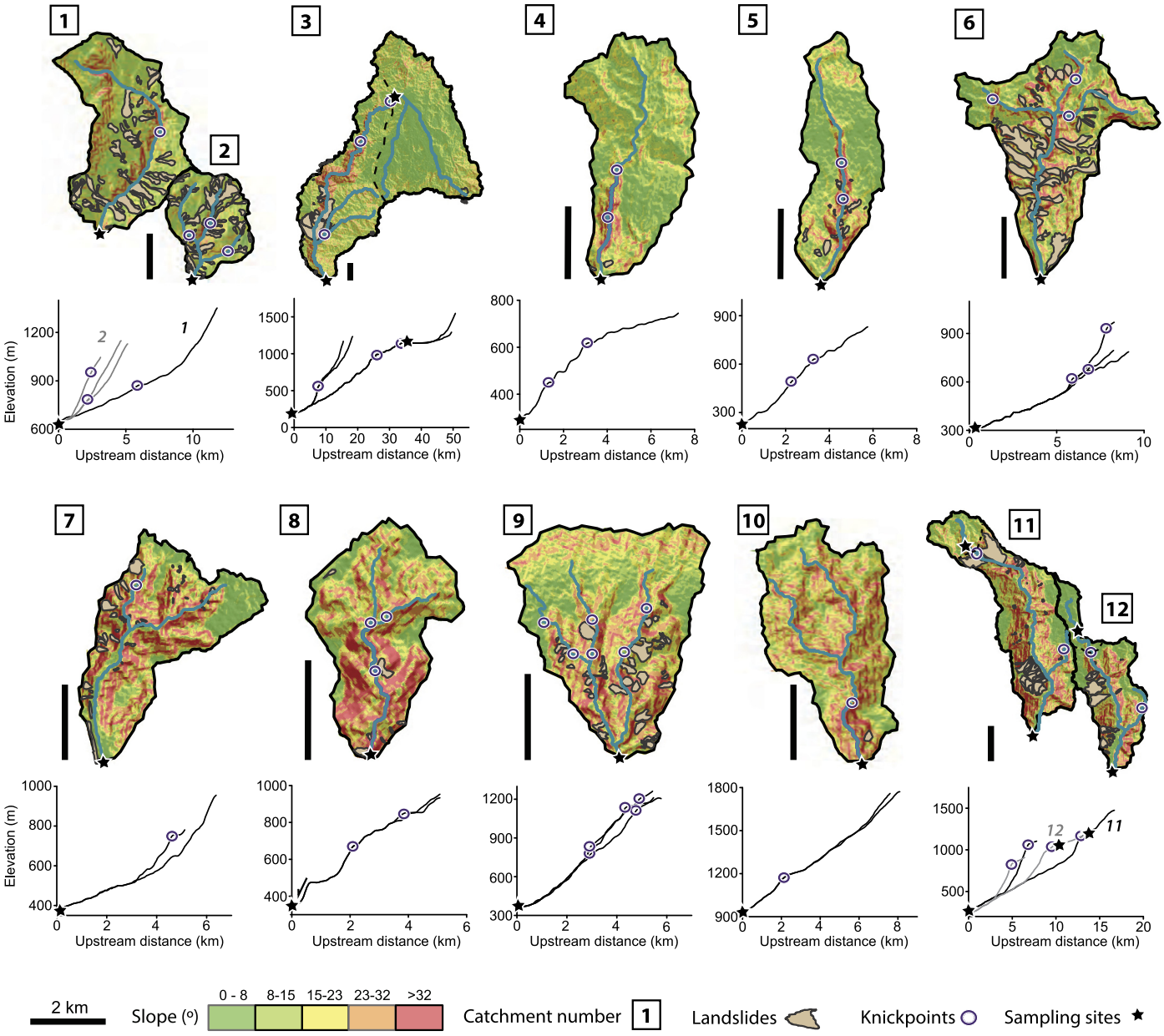

Fig. 2. Slope maps of the sampled catchments, and river long profiles of the main channels draining them, with the identified knickpoints and landslides. Incision maps used to estimate maximum incision and minimum eroded volumes, derived from the same DEM, are available in the supplementary material.

catchment (i.e. maximum local relief), as a measure of the amplitude of the transient response to tectonics (Table 1). This metric is more representative of the geomorphology of the landslide-prone areas below the knickpoints and the response to active tectonics than total catchment relief or mean slope, given that the catchments have different amounts of inherited, pre-faulting relief (Roda-Boluda and Whittaker, 2017, 2018). Minimum time-averaged incision rates are obtained by dividing this maximum incision by 1 Myr, the time since incision below the knickpoints started. Incision maps and minimum catchment eroded volumes (used for estimating minimum sediment fluxes, below) were derived by creating a TIN surface capping the catchment around the drainage divide and subtracting the clipped catchment DEM from this surface (see supplementary material). Slope maps (Fig. 2) and catchment mean slope are derived from the same ASTER DEM.

3.4. Landslides

To infer the numbers and volumes of landslides (Table 1), we use the landslide maps presented in Fig. 2, and the $V = 0.253A^{1.284}$ landslide area (A)–volume (V) scaling relationship, both previously published by Roda-Boluda et al. (2018) (see also supplementary information). We choose this geomorphological landslide inventory because it covers all of our study area and it likely integrates landscape response over a more similar timescale (10^2–10^3 yrs) to CRN data than available multi-temporal inventories (10^0–10^1 yrs, see supplementary material). The frequency-area distribution of this inventory suggests that landslides <0.04 km^2 may be under-represented (see supplementary information). The time period of cumulative landsliding that the inventory represents must be similar to: (a) how long the biggest landslides are stored in the hillslopes before they are eroded or re-vegetated; and (b) to the time that would be required for the observed landslide

Table 1
Tectonic and geomorphologic characteristics of the sampled catchments. Catchment numbers are those shown in Fig. 1 and Fig. 2.

Catchment number	Catchment area (km^2)	Catchment uplift rate at fault (mm/yr)	Steady-state sediment flux ($\times 10^3$ m^3/yr)	Knickpoint height above the fault (m)		Maximum depth of incision (m)	Minimum eroded catchment volume ($\times 10^7$ m^3)[a]	Minimum sediment flux from eroded volume (m^3/yr)[b]	Number of landslides on catchment	Area covered by landslides (km^2)	% of catchment area affected by landslides	Volume of landslides stored on catchment ($\times 10^4$ m^3)[c]	Normalised landslide volume (m)
				Lower	Upper								
1	32.12	0.27 ± 0.05	8.8 ± 1.6	311 ± 86		408 ± 28	254	2536	63	5.45	17.0	4032 ± 960	1.26 ± 0.30
2	13.33	0.27 ± 0.05	3.6 ± 0.7	252 ± 85		237 ± 28	94	938	60	3.52	26.0	2313 ± 541	1.73 ± 0.41
3	288.31	0.44 ± 0.19	127.4 ± 55.1	548 ± 176	940 ± 28	587 ± 28	210	2100	51	10.64	3.7	14453 ± 3807	0.50 ± 0.13
3 upstream	155.30	–	–			300 ± 28	1173	11728	–	–	–	–	–
4	15.84	0.31 ± 0.08	5.0 ± 1.3	179 ± 28	341 ± 28	219 ± 28	101	1008	6	0.33	2.1	229 ± 54	0.14 ± 0.03
5	11.34	0.36 ± 0.10	4.0 ± 1.1	223 ± 28	371 ± 28	211 ± 28	24	235	20	0.76	6.7	176 ± 27	0.16 ± 0.02
6	21.84	0.44 ± 0.12	9.6 ± 2.6	407 ± 174		353 ± 28	198	1984	52	6.70	30.7	3264 ± 121	1.49 ± 0.06
7	13.53	0.48 ± 0.13	6.5 ± 1.8	363 ± 28		386 ± 28	118	1181	39	0.67	4.9	329 ± 73	0.24 ± 0.05
8	8.58	0.59 ± 0.16	5.0 ± 1.4	344 ± 28	505 ± 28	331 ± 28	88	879	9	0.13	1.6	62 ± 14	0.07 ± 0.02
9	16.64	0.66 ± 0.18	11.0 ± 3.0	430 ± 35	674 ± 85	358 ± 28	189	1892	42	1.03	6.2	544 ± 122	0.33 ± 0.07
10	15.55	0.51 ± 0.14	7.9 ± 2.1	239 ± 28		305 ± 28	150	1497	1	0.01	0.1	2 ± 1	0.001 ± 0.0006
11	39.37	0.72 ± 0.19	28.2 ± 7.6	806 ± 45		563 ± 28	192	1919	48	5.16	13.1	5278 ± 1328	1.34 ± 0.34
11 upstream	2.30	–	–			120 ± 28	2	15	–	–	–	–	–
12	22.92	0.60 ± 0.16	13.7 ± 3.7	635 ± 41		466 ± 28	98	978	23	1.95	8.5	1653 ± 403	0.72 ± 0.18
12 upstream	3.15	–	–			36 ± 28	2	23	–	–	–	–	–
Median	15.84	0.46 ± 0.14	6.5 ± 1.6					1181	40.5	1.49	6.5	1099 ± 121	0.41 ± 0.05

[a] Derived from incision maps, see methods and supplementary information.
[b] From the minimum eroded catchment volume, divided by 1 Myr (time since faulting/incision initiation).
[c] Calculated for individual landslides using the field-based, area-volume scaling relationship for the study area, $V = 0.253A^{1.284}$ (Roda-Boluda et al., 2018; see also supplementary information), and summing the volume.

Table 2
Sample collection data, ^{10}Be analytical results, and calculated erosion rates.

Sample and catchment number	Latitude (°North)	Longitude (°East)	Catchment effective elevation (m)[a]	Topographic shielding factor	^{10}Be (10^3 atoms/g qtz)[b]	Production rate (muogenic) (atoms/g/yr)[c]	Production rate (spallogenic) (atoms/g/yr)[c]	Erosion rates (mm/yr)[d]	Internal uncertainty (mm/yr)	External uncertainty (mm/yr)	^{10}Be erosional timescale (yrs)[e]	% of above-background erosion	^{10}Be-derived sediment flux (m^3/yr)	Landslide inventory timescale if landslides supply 35% of sediment flux (yrs)[f]	Landslide inventory timescale if landslides supply 85% of sediment flux (yrs)[g]
1	40.329972	15.913611	1084	0.99	24.93 ± 1.28	0.11	9.31	0.27	0.01	0.02	2258 ± 123	63.5 ± 1.8	8535 ± 440	13498	5558
2	40.290972	15.951222	1004	0.99	42.87 ± 2.04	0.11	8.78	0.15	0.01	0.01	4117 ± 207	33.4 ± 3.0	1943 ± 93	34010	14004
3	39.478056	16.253889	1166	0.99	21.96 ± 1.45	0.11	9.82	0.32	0.02	0.03	1895 ± 135	69.4 ± 1.9	91306 ± 6072	4523	1862
3 upstream	39.403139	16.535139	1294	1.00	44.95 ± 2.21	0.12	10.85	0.17	0.01	0.02	3567 ± 185	42.3 ± 2.7	26121 ± 1291	–	–
4	38.627472	16.227750	703	0.99	50.03 ± 2.42	0.10	6.72	0.10	0.00	0.01	6097 ± 313	8.5 ± 2.5	1559 ± 76	4202	1730
5	38.550889	16.152611	708	0.99	14.13 ± 2.44	0.10	6.72	0.35	0.06	0.07	1694± 369	72.6 ± 4.2	4018 ± 718	1254	516
6	38.420861	16.098972	719	0.97	11.13 ± 1.22	0.10	6.65	0.45	0.05	0.06	1342 ± 168	78.3 ± 2.2	9760 ± 1086	9553	3934
7	38.343194	16.066389	752	0.97	11.80 ± 1.87	0.10	6.77	0.43	0.07	0.08	1403 ± 273	77.3 ± 3.2	5786 ± 942	1624	669
8	38.299778	16.003667	891	0.97	27.64 ± 2.91	0.10	7.55	0.20	0.02	0.03	3013 ± 361	51.3 ± 4.7	1708 ± 183	1033	425
9	38.250222	15.955917	1039	0.97	21.52 ± 2.52	0.11	8.49	0.28	0.03	0.04	2110 ± 286	65.9 ± 3.6	4731 ± 564	3286	1353
10	38.211917	15.882028	1530	0.97	29.18 ± 2.55	0.13	12.27	0.29	0.03	0.03	2062 ± 199	66.7 ± 2.7	4526 ± 399	16	6
11	38.083500	15.727111	1079	0.97	9.90 ± 1.15	0.11	8.72	0.64	0.08	0.09	944 ± 127	84.7 ± 1.6	25035 ± 2964	6023	2480
11 upstream	38.118083	15.842778	1585	0.99	88.75 ± 3.43	0.13	12.94	0.10	0.00	0.01	6031 ± 245	2.5 ± 3.7	229 ± 9	–	–
12	38.047083	15.696722	819	0.97	36.49 ± 11.55	0.10	7.12	0.14	0.05	0.05	4199 ± 2303	32.1 ± 17.8	3275 ± 1160	14425	5940
12 upstream	38.063111	15.785250	1139	1.00	79.87 ± 4.99	0.11	9.40	0.08	0.01	0.01	7274 ± 491	0.0	259 ± 16	–	–
Median							8.72	0.27			2258 ± 245		4526 ± 564	4362	1796

[a] Elevation that generates the spallation production rate that corresponds to the hypsometry-weighted production rate for the catchment.
[b] Ratios normalised to the NIST_27900 isotope ratio standard with a ^{10}Be/^{9}Be ratio of 2.79×10^{-11}. Assumed ^{10}Be half-life of 1.36 Myr. The subtracted process blank ^{10}Be/^{9}Be ratio is 1.98×10^{-15} (405.4 ppm carrier). The errors represent the propagated 1σ analytical uncertainty of the AMS measurements and blank correction.
[c] Calculated with Cronus 2.3. calculator, based on the constant production rate model of Lal (1991)/Stone (2000) and a 4.01 atoms/g/yr reference production rate for neutron spallation (Borchers et al., 2016).
[d] Based on an assumed bedrock density of 2.6 g/cm^3.
[e] Time required to remove one mean attenuation path length, $T = z^*/e$, using $z^* = 60$ cm (typical for silicate rocks).
[f] Calculated as: landslide volume/(^{10}Be sediment flux × 0.35).
[g] Calculated as: landslide volume/(^{10}Be sediment flux × 0.85).

volumes to have accumulated at rates that match long-term landslide sediment fluxes. There is no direct information on (a) for the area, so we estimate plausible landslide inventory timescales by dividing the total volume of landslides stored in catchments by a fraction of the ^{10}Be-derived sediment fluxes (i.e. inferred landslide sediment fluxes; Table 2).

3.5. Numerical model implementation

We use the calculated ^{10}Be erosion rates and the observed number of landslides to investigate plausible landslide recurrence intervals and sediment mixing conditions (i.e. extent of mixing and hillslope vs. fluvial mixing) for the study area, by implementing the numerical model of Yanites et al. (2009). The first part of the model generates an erosional scenario for a catchment of area A_b, based on a background erosion rate, E_b, and a stochastic landslide model constrained by: minimum and maximum landslide areas, $A_{\min}$ and $A_{\max}$; the power law exponent of the cumulative frequency-area scaling, β_c; a landslide area-depth scaling coefficient, ε; and the recurrence interval of landslides, R_i (years between successive landslides in a 1 km^2 parcel). These parameters are extracted from the landslide inventory of Roda-Boluda et al. (2018), and presented in Section 2 and Table 3. The landslide recurrence interval, R_i, is unknown, so we run the model for 23 different R_i values between 500 yrs/km^2 and 2×10^4 yrs/km^2. Background erosion rates, E_b, are obtained from our results. Because our goal is to obtain general insight into landslide dynamics in the study area, we run the model for an hypothetical catchment with $A_b = 16$ km^2, the median size of the studied catchments (Table 1 and 3). We run the model for 50 kyr to remove the effects of the initial conditions, as suggested by Yanites et al. (2009), followed by additional periods of 2 kyr and 7 kyr (the median and maximum erosional timescale values that our ^{10}Be samples represent, respectively; Table 2 and 3) in which the model continues to run and its results are captured. For every scenario, a different volumetric erosion rate value can be obtained in each run, since the landslide model is a Poisson-based stochastic model, so we run each scenario 6 times for each capture time (2 and 7 kyr). Since we find no systematic differences in using these two capture times, we subsequently combined all the model runs. The output of this part of the model is a "true", volumetric, long-term erosion rate, E_{rv}; and a number of ^{10}Be atoms added to the fluvial system at different time steps (based on the CRN production parameters specified in Table 3), which feeds the second part of the model.

The second part of the model calculates, from the ^{10}Be concentrations produced in the first part and the potential sediment mixing time, τ, the probability that fluvial sediment samples yield ^{10}Be concentrations that provide erosion rate estimates within a chosen threshold of long-term ones, 50% in our case (i.e. the accuracy of the ^{10}Be erosion rates with respect to the "true" erosion rates). In its original set up, the model uses A_b as a scaling variable to predict: the width, depth, and volume, V, of fluvial sediment stored within the catchments; catchment sediment flux, Q_{sed}; and from these, the residence time of sediment on the fluvial reservoir (equal to the maximum potential mixing time), τ ($\tau = V/Q_{sed}$). This original model set up assumes that sediment mixing only happens through fluvial storage. Justification on how these parameters are obtained from A_b can be found in Yanites et al. (2009). For each erosional scenario run on the first part, we operate the second part of the model under this fluvial-exclusive mixing scenario, and under two scenarios that assume most sediment mixing occurs on the hillslopes as landslide deposits are eroded progressively, for minimum and maximum plausible "hillslope reservoir" τ values (Table 3). To calculate τ for the maximum $\tau_{\max}$ "hillslope reservoir" scenario, we use as V the median value of landslide volumes on the catchments (i.e. "switching" modelled fluvial sediment storage by observed hillslope sediment storage on landslide deposits), and as Q_{sed}, the median value obtained by dividing the eroded catchment volumes by 1 Myr, assumed to be a minimum, long-term sediment flux estimate (Tables 1 and 3). For the minimum $\tau_{\min}$ "hillslope reservoir" scenario, we use half of the V used above (i.e. considering that only 50% of landslide sediment stored on the hillslopes is effectively mixed), and a Q_{sed} of ~50% the median value of the steady-state-based sediment flux (Tables 1 and 3), in agreement with later findings. Table 3 provides a summary of these input parameters.

4. Results

4.1. ^{10}Be catchment-averaged erosion rates and normal faulting

Catchment-averaged erosion rates range between 0.08 and 0.64 mm/yr, with those of the unincised, low-relief, upper catchments above knickpoints lying in a narrow range of 0.08 to 0.17 mm/yr (Fig. 1 and 2). Upstream of knickpoints, in the low-relief plateau of the Sila massif, Olivetti et al. (2012) obtained five ^{10}Be-erosion rates ranging from 0.07 to 0.10 mm/yr (Fig. 1c). The combined eight samples suggest that these undisturbed sub-catchments, not yet affected by incision, are eroding at consistent rates of $0.09^{+0.08}_{-0.02}$ mm/yr. Catchment-averaged erosion rates have the same order of magnitude as the fault throw rates (Fig. 3, Tables 1, 2). Of the samples collected at the catchment outlets, 75% have erosion rates that are within a factor of 2 of the footwall throw rates estimated at the catchment position, and 50% have identical values to the fault throw rate, within the error range of both estimates (Fig. 3).

Erosion rates are generally higher for catchments affected by faster fault throw rates, and for an intercept at 0.1 mm/yr (the erosion rate for the upstream 'relict' landscapes, that have not responded yet to tectonics, with a 0 mm/yr virtual throw rate value), a linear correlation would indicate that erosion is overall removing ~50% of the material being uplifted by the faults, although some catchments are closer to achieving steady-state (Fig. 4a). The scatter in this plot (Fig. 4a) could be due to the uncertainties in our throw rate estimates and their timescales (of ~1 Myr, in comparison to the 10^2–10^3 yr CRN timescales), to the inherent variability of CRN measurements in landslide-prone areas, and/or differences in lithology, Generally, samples from granitic catchments have higher erosion rates than catchments draining metamorphic rocks, for similar throw rates (Fig. 4a). We compare our ^{10}Be-erosion rates with those of Cyr et al. (2010) from coastal catchments for which regional rock uplift rates are known, and observe that two of their three data points fall perfectly on our derived erosion-uplift scaling (the other is the only datum out of 38 implying erosion rates >1 mm/yr), supporting that higher uplift rates drive higher erosion rates (Fig. 4a inset).

4.2. Transient erosional response to normal faulting

Our erosion rate data must be considered in the context of transient landscape response to active normal faulting (Fig. 2). The elevations above the fault of the highest knickpoint in each catchment are linearly correlated with fault throw rates (Fig. 4b, Table 1). All these upper knickpoints developed at ~1 Ma (see Section 2; Roda-Boluda and Whittaker, 2017, 2018), so we hypothesise that their markedly different elevations are related to fault-controlled differences in knickpoint vertical propagation rates (Wobus et al., 2006; Whittaker et al., 2008; Attal et al., 2011), which are similar to the fault throw rates (Fig. 4b right-axis). Maximum incision depths in the catchments range from ~200 to 600 m, and between ~36 and 300 m for the sub-catchments above knickpoints, (Table 1; Fig. 2, Fig. 4c), and incision and incision rates

Table 3
Input parameters for the different erosional and mixing scenarios tested using the Yanites et al. (2009) model. Tables with the results of all model runs, presented in Fig. 7, can be found in the supplementary material.

Parameter	Input value	Derived from
CosmoLand (erosional model) parameters		
Catchment area (A_b)	16 km^2	Median area of the studied catchments
Maximum landslide area (A_{max})	580 m^2	From Roda-Boluda et al. (2018); see also supplementary material
Minimum landslide area (A_{min})	3.7×10^6 m^2	From Roda-Boluda et al. (2018); see also supplementary material
Landslide cumulative frequency-area distribution exponent ($\beta_c = \beta - 1$)	1.3	From Roda-Boluda et al. (2018); see also supplementary material
Landslide area-depth scaling coefficient (ε)	0.015	Based on $\varepsilon = d/A^{1/2}$, where d is landslide scour depth and A is landslide area (as in Yanites et al., 2009). We use the values of the median-sized landslide of the regional inventory from Roda-Boluda et al. (2018); $\varepsilon = 2.3$ m/$(2.5 \times 10^4)^{1/2}$ m
Landslide recurrence interval (R_i)	23 values between 500 yrs and 20 kyrs	Used as main variable, see also supplementary material.
Background erosion rate (E_b)	0.10 mm/yr	Fig. 1 and 5; this work's results and Olivetti et al. (2012)
Model and capture times	52 kyrs (50 kyrs set-up run + 2 kyrs capture time); 57 kyrs (50 kyrs set-up run + 7 kyrs capture time)	Set-up model time as suggested in Yanites et al. (2009); capture times from median and maximum value of the erosional timescale of this work's samples (Table 2)
Cosmogenic nuclide production parameters	$\rho = 2.6$ g/cm^3; Production rate = 9 at/g/yr	Density used to calculate erosion rates in this work, and median production rate for the studied catchments (Table 2). Other production parameters are standard and kept as in Yanites et al. (2009)
SedMix (sediment mixing model) parameters		
Critical drainage area needed to maintain a channel (A_c)	10^5 m^2	Based on field observations on the study area; reported in Roda-Boluda and Whittaker (2017, 2018)
Fluvial-only mixing scenario: sediment reservoir variables calculated by SedMix from catchment area A_b		
Sediment storage volume (V)	~0 m^3	Calculated from A_b by SedMix model as in Yanites et al. (2009). For a full derivation of the equations that estimate V, Q_{sed} and M_t based on A_b, and the parameters used, the reader is referred to the original paper.
Sediment flux from the catchment (Q_{sed})	4.16×10^9 m^3/yr	Same
Residence time of sediment on the reservoir (τ)	~0 yrs	Same
Hillslope mixing scenarios: sediment reservoir variables used in maximum/minimum potential sediment mixing times, M_t		
Sediment storage volume (V)	1.1×10^7 m^3; 5.5×10^6 m^3	Median value of total stored landslide volume on the studied catchments; half that value
Sediment flux from the catchment (Q_{sed})	1000 m^3/yr; 3000 m^3/yr	Median of the minimum sediment flux estimate from eroded catchment volumes (Table 1); 50% of median value of the steady-state based sediment fluxes (Fig. 4a)
Residence time of sediment on the reservoir (τ_{max}/τ_{min})	11 kyrs; 1.8 kyrs	$\tau = V/Q_{sed}$

are greater for catchments affected by greater fault throw rates (Fig. 4c). Therefore, normal faulting is clearly controlling landscape transient response via knickpoint retreat and associated fluvial incision, and the rates of these three processes have nearly identical values to the ^{10}Be erosion rates. Comparison of the ^{10}Be results from up- and downstream of knickpoints shows that the transient wave of incision is associated with erosion-rate increases of a factor of ~2–6 times (Figs. 3 and 4, Table 2), in agreement with the findings of Olivetti et al. (2012) documenting a ~3–6-fold increase in erosion rates below knickpoints (Fig. 1).

Erosion rates increase non-linearly with catchment maximum incision, i.e. a measure of transient adjustment (Fig. 5a). Given that ~0.10 mm/yr appears to be the consistent background erosion rate in the absence of incision (Fig. 4a and 4c), we can estimate the proportion of the catchment-averaged erosion rates that could be attributed to landscape response to tectonics, by calculating the proportion of the ^{10}Be erosion rate above this background value (Fig. 5a right y-axis, Table 2). This proportion of "above-background" erosion rate ranges between 0% (at the relict surfaces) to 85%, increasing with incision, and is >35% for most below-knickpoint samples. Catchment erosion rates also increase with increasing mean catchment slope (Fig. 5b), albeit less non-linearly, likely because mean slopes also encapsulate variable proportions of unadjusted areas above knickpoints (Fig. 2). These correlations suggest that ^{10}Be catchment-averaged erosion rates are capturing the transient incisional and hillslope steepening response to normal faulting.

Between 9 and 63 landslides have been identified in the incised sectors of the catchments, occupying 2 to 30% of the catchment areas, while none are found on the low-relief, unincised subcatchments (Fig. 2, Table 1). Estimated volumes of landslides stored in these catchments range between 2 km^3 and 14.5×10^7 km^3 (Table 1). Both the total volume (Fig. 5c) and number (Fig. 5d) of landslides increase non-linearly with the degree of catchment incision. Landsliding becomes significant where catchment incision exceeds ~200 m, similar to the point where Fig. 5a records the non-linear increase in erosion rates. Therefore, both landsliding and ^{10}Be catchment-averaged erosion rates are governed by the extent of upstream-migrating incision and subsequent hillslope steepening (Fig. 5), which are controlled by the rates of normal faulting (Fig. 4). Hence, ^{10}Be erosion rates would be expected to correlate with landslide erosion and sediment fluxes.

4.3. ^{10}Be-derived sediment fluxes and landsliding

^{10}Be-derived sediment fluxes range between 0.23 m^3/yr and 9.13×10^4 m^3/yr (Table 2). Catchments with greater ^{10}Be-sediment flux have consistently larger volumes of stored landslide material (Fig. 6a, also suggested by comparison of Fig. 5a and 5c). However, converting landslide volumes into landslide-derived sediment fluxes is non-trivial. The volumes of landslides stored in

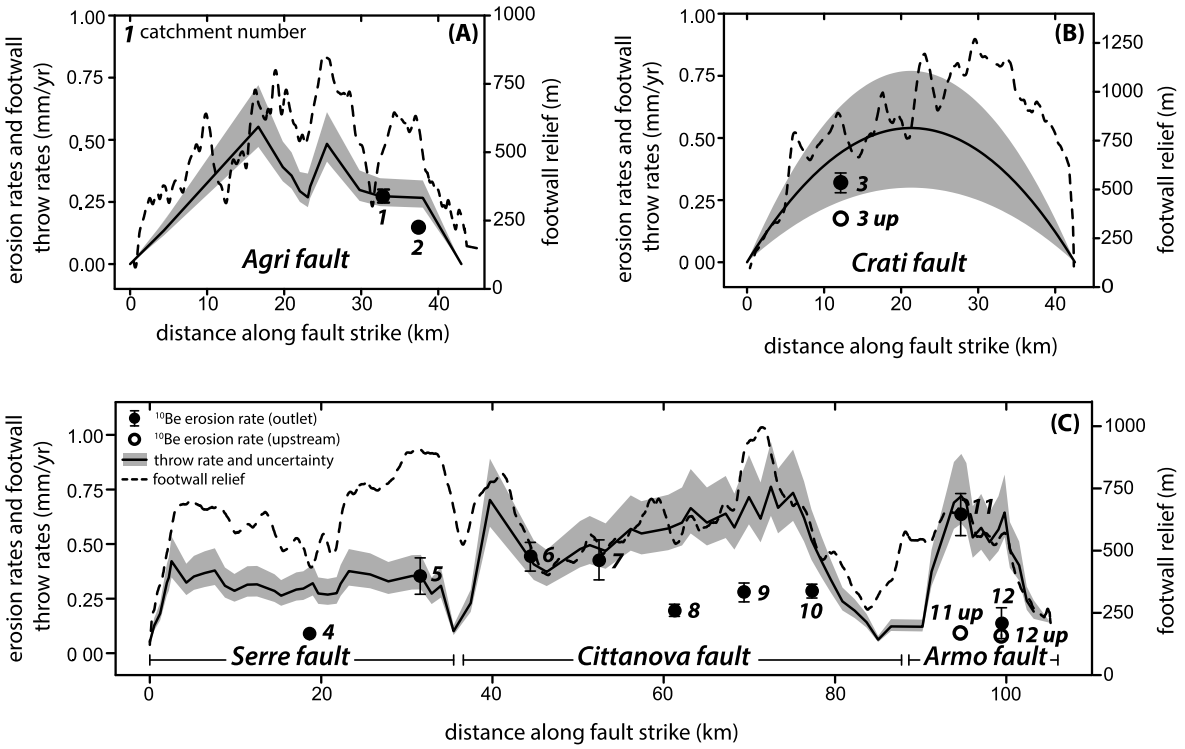

Fig. 3. Profiles of the footwall component of fault throw rates and footwall relief along the studied faults, and ^{10}Be erosion rates plotted at the along-strike distance where the catchment outlets are. (a) Agri fault, Basilicata; (b) Crati fault, northern Calabria; and (c) Serre, Cittanova and Armo faults, southern Calabria. Catchment numbers correspond to those shown in Figs. 1 and 2. The key in (c) applies to the three graphs. Throw rate and footwall relief data have been extracted from Roda-Boluda and Whittaker (2017, 2018).

these catchments represent a "snapshot" of landsliding that is the result of the landslide rate, removal of landslide material, and the time that the landslide inventory represents; the latter of which is unconstrained. Therefore, estimating landslide sediment fluxes requires some assumptions. The proportion of catchment erosion linked to transient incision and landsliding is between 35 and 85% (Fig. 5a, Table 2). If, for instance, catchments had landslide sediment fluxes that were 85% of the ^{10}Be-derived sediment fluxes, then to produce the estimated volumes of landslides on the catchments, these landslide fluxes would need to have operated over timescales of 6 yrs to 14 kyrs, with a median timescale of ~1.8 kyrs (Table 2). Similarly, if landslide fluxes were 35% of the ^{10}Be-derived sediment fluxes, between 16 yrs and 34 kyrs would have been needed to accumulate the estimated landslide volumes on different catchments, with a median landsliding timescale of ~4.4 kyrs (Table 2). These landslide inventory timescales are minimum estimates, because the real volumes of landslides accumulated are probably greater than we can infer from our inventory, which cannot account for the landslides that have been completely eroded. Based on these first-order estimates, sediment flux from landslides would be on the order of 10^3 to 10^4 m^3/yr (Fig. 6a, right axis).

To account for the fact that bigger catchments may have more landslides, we plot ^{10}Be erosion rates against landslide volumes normalised by catchment area, and against the % of catchment area affected by landsliding (Table 1, Fig. 6b). These trends suggest that the relation between ^{10}Be erosion rates and landsliding is robust, although there is significant scatter that could be due to the stochastic nature of landsliding, the inherent uncertainties of any landslide or CRN data set, and lithology. Indeed, catchments draining flysch sandstones have higher normalised volumes and % of area affected by landslides for a given ^{10}Be erosion rate than the overall trend, in agreement with previous work that shows that flysch sandstones are about twice as prone to landsliding compared to other lithologies in the area (see Section 2; Roda-Boluda et al., 2018). Normalised landslide volumes entail considerable catchment-average thicknesses of landslide material between 0.07–1.73 m. Overall, ^{10}Be erosion rates increase with measures of landslide erosion (Figs. 5 and 6), suggesting that landslides are a major source of sediment and significantly influence ^{10}Be concentrations.

4.4. ^{10}Be-erosion rate accuracy and landslide and sediment mixing dynamics

In landslide-prone areas, noisy data sets with numerous outliers have been predicted by numerical models (Niemi et al., 2005; Yanites et al., 2009) or suggested by empirical data (Densmore et al., 2009; Stock et al., 2009). In our study area, 37 out of 38 ^{10}Be erosion rates fall in the range of $0.39^{+0.42}_{-0.33}$ mm/yr (Fig. 1), a relatively narrow one for landslide-dominated areas (e.g. Niemi et al., 2005). Additionally, where fault throw rates or regional uplift rates are available, ^{10}Be erosion rates are well-correlated with them (Fig. 4a; Cyr et al., 2010). Therefore, landslide activity does not add substantial noise to ^{10}Be erosion rates in the area; instead, ^{10}Be erosion rates document the increase in landslide activity as incision progresses (Figs. 5 and 6), while still correlating with the fault throw rates that determine this transient response (Fig. 4). Consequently, we proceed under the assumption that our ^{10}Be erosion rates adequately reflect long-term erosion rates, and explore the plausible landslide recurrence intervals, R_i, and sediment mixing conditions (degree of mixing and hillslope vs. fluvial mixing) that must be fulfilled for this to occur, by implementing Yanites et al. (2009) numerical model as described in section 3.1, with input parameters listed in Table 3.

For a background erosion rate, E_b, of 0.1 mm/yr (Figs. 1, 4 and 5), R_i values of between 5–18 kyrs/km^2 would be required for the mean long-term, volumetric erosion rates (E_{rv}) to approx-

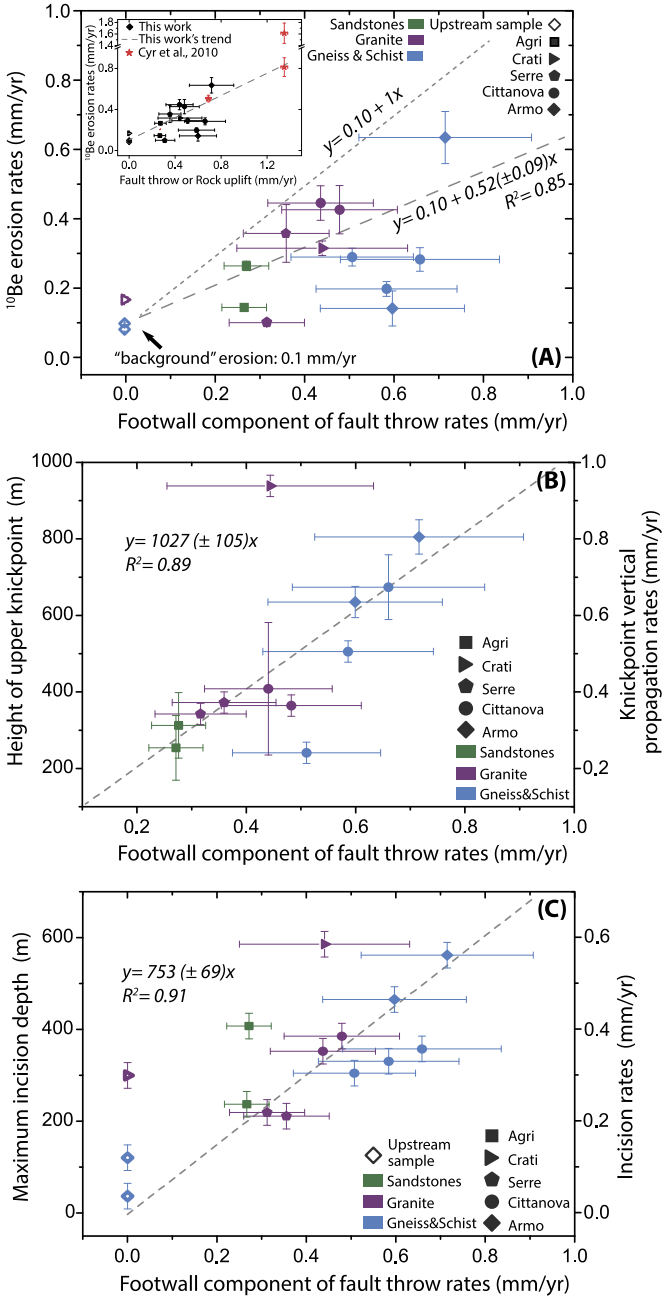

Fig. 4. (a) ^{10}Be catchment-averaged erosion rates, plotted against the footwall component of fault throw rates estimated for each catchment. The inset shows the same data as the main figure (in black), together with paired ^{10}Be erosion rates and regional rock uplift rates from Cyr et al. (2010), collected in southern Calabria (Fig. 1d). (b) Height above the fault of the upper (or single) knickpoint in the catchment, plotted against the footwall component of fault throw rates estimated for the catchment. (c) Maximum incision against the catchment footwall throw rate. The right y-axis on (b) and (c) shows the equivalent knickpoint vertical propagation, and incision rates, if knickpoint migration and incision started ~1 Ma (see section 2). All plotted values can be found in Tables 1 and 2.

imate the values encompassed between the 25th–75th percentiles of the 37 consistent ^{10}Be erosion rate values measured in the area (Fig. 7a). Additional constraints on plausible R_i values can be derived by comparing the number of landslides observed on the catchments (Table 1, Figs. 2 and 5) and the maximum number of landslides (i.e. assuming no removal of landslide material) that would be expected in a 16 km^2 catchment for each R_i value, considering the landslide inventory timescales suggested by Fig. 6a and Table 2 of 1.8–4.4 kyr (±20% uncertainty). In this case, R_i values between 0.5–6 kyr/km^2 would be needed to explain the 25th–75th percentiles of the number of landslides observed in the catchments (Table 1, Fig. 2). Based on the overlap of R_i values deduced from Figs. 7a and 7b, a long-term, time-averaged R_i value of the order of 5–6 kyrs/ km^2 would be most likely.

The second part of the model evaluates which R_i values and sediment mixing conditions would be required for our ^{10}Be-derived rates to be accurate. For the fluvial-exclusive mixing scenario, the model predicts that reliable samples could only be obtained if $R_i \geq 15$ kyrs (Fig. 7c), which is not supported by Figs. 7a and 7b. Therefore, given the limited potential for fluvial storage that these catchments have due to their small size, the fluvial reservoir cannot adequately mix sediment to produce ^{10}Be samples representative of E_{rv} values. This is supported by field observations of very moderate fluvial coverage on prominently bedrock channels. In contrast, field observations and our results (Fig. 6a, Table 2) indicate that landslide deposits are likely stored on hillslopes for ~10^1–10^3 yrs (i.e. similar to the landslide inventory timescale, see Methods). We hypothesise that sufficient sediment mixing within our catchments could take place as runoff regularly strips off the top mm–cm of each landslide deposit stored on the hillslopes, particularly the suspended sediment fraction that we have sampled. We test this hypothesis by modelling two possible sediment mixing scenarios in the "hillslope reservoir". For the first, we use a maximum sediment mixing time, τ_{max}, for this reservoir derived from the median value of landslide volumes on the studied catchments, $V = 1.1 \times 10^7$ m^3, and $Q_{sed} = 1000$ m^3/yr (minimum, long-term Q_{sed} estimate; see Section 3.1, and Tables 1 and 3). For the second, minimum τ_{min} "hillslope reservoir" scenario, we use half of the V used above, $V = 5.5 \times 10^6$ m^3 (i.e. considering that only 50% of landslide sediment stored on hillslopes is mixed effectively), and $Q_{sed} = 3000$ m^3/yr, given by ~50% of median value of the steady-state-based Q_{sed} (Table 1), in agreement with findings of Fig. 4a that indicate that overall erosion rates are ~50% of the throw rates. The corresponding plausible τ for the hillslope storage scenarios would be $\tau_{max} = 11$ kyrs and $\tau_{min} = 1.8$ kyrs ($M_t = V/Q_{sed}$, Table 3). In both cases, the likelihood of obtaining accurate ^{10}Be erosion rates are >50% when $R_i > 10$ kyr/km^2 (Figs. 7c). The median probability of obtaining ^{10}Be concentrations that represent E_{rv} would be 30–40% for $R_i = 5$ kyrs/km^2, and 40–70% for $R_i = 6$ kyrs/km^2 (Figs. 7c). Although in reality the studied catchments probably have different landslide frequencies dictated by their different incisional responses, to a first-order, a R_i ~6 kyrs/km^2 seems to explain well the range of erosion rates and numbers of landslides detected in the study area (Fig. 7a and b), and can produce accurate ^{10}Be samples, as long as most sediment mixing takes place while landslides are stored on the hillslopes (Fig. 7c).

5. Discussion

5.1. Active faulting, transient response, and catchment-averaged erosion rates

Our data show that catchment-averaged erosion rates are controlled by fault throw rates and the degree of landscape adjustment to those rates, with stronger lithologies eroding at slightly lower rates, and weaker ones at slightly higher rates (section 2, Table 2, Figs. 3 and 4a). This study provides, to our knowledge, the first robust empirical evidence that along normal faults, differences in fault throw rates are reflected in catchment-averaged erosion rates. Some key differences between our study and previous ones evaluating CRN erosion rates along normal faults (Stock et al., 2009; Densmore et al., 2009) are that we exploit very detailed throw rate constraints, and that we have characterised the

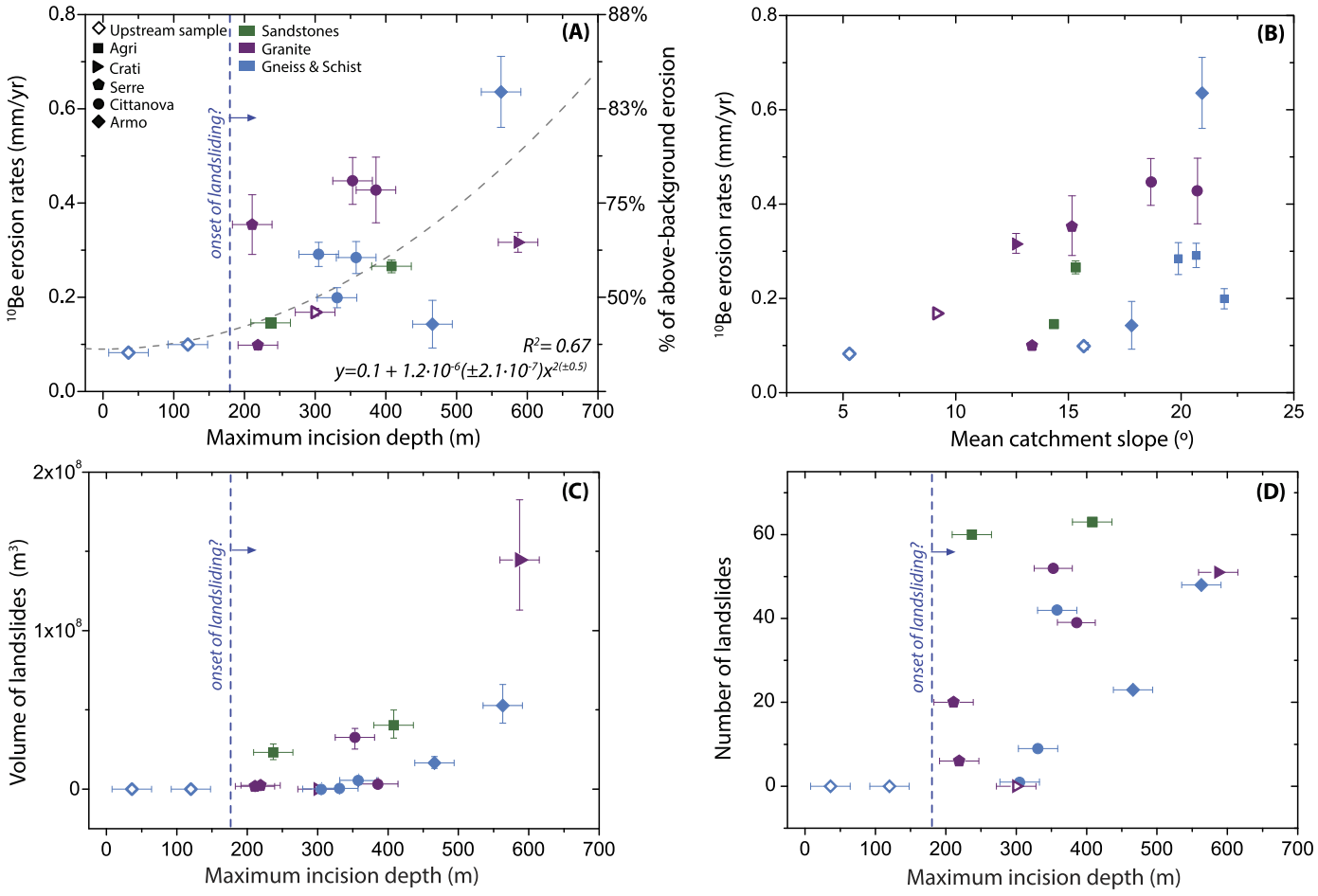

Fig. 5. (a) ^{10}Be catchment-averaged erosion rates (left *y*-axis) and percentage of above-background erosion (right *y*-axis) against maximum catchment incision. The right *y*-axis has non-linear numbering because linear increments in erosion rates correspond to non-linear increments in percentage above background erosion (i.e. for an erosion rate of 0.2 mm/yr, the background erosion rate of 0.1 mm/yr represents 50% of the total erosional budget; while for 0.6 mm/yr, 83% of the erosional budget cannot be explained by the 0.1 mm/yr background erosion rate). (b) ^{10}Be erosion rates against catchment mean slopes. (c) Total volume of landslides stored in the catchments against catchment maximum incision. (d) Number of mapped landslides against maximum incision on catchment. The symbol and colour key in (a) applies to (b), (c) and (d).

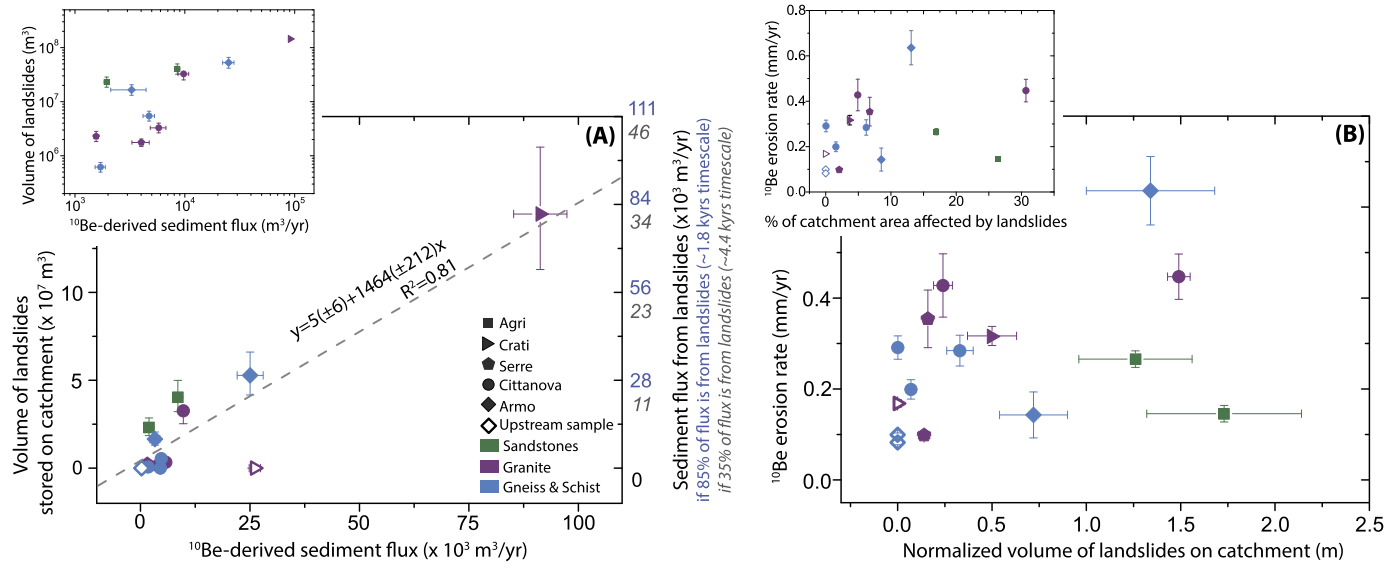

Fig. 6. (a) Volume of landslides stored on catchments (left *y*-axis), plotted against sediment flux estimates derived from the ^{10}Be erosion rates and catchment areas. On the right axis, landslide volumes are converted into sediment flux estimates based on two scenarios where landslides supply 35% and 85% of the total sediment fluxes. For the landslide volumes to represent 35% of the ^{10}Be-derived sediment fluxes, the mapped landslides should represent landsliding over ~4.4 kyrs; and if landslides supply 85% of the fluxes, the landsliding timescale should be ~1.8 kyrs. The inset graph shows the same data with logarithmic axis. (b) ^{10}Be erosion rates plotted against the volume of landslides normalised by catchment area (Table 1). The inset graph shows ^{10}Be erosion rates plotted against the % of catchment area affected by landslides (Table 1), another way of account for the effects of catchment area.

catchments' transient responses, including landsliding. Additionally, earthquake recurrence times for our studied faults range between ~0.3–3.0 kyr (e.g. Valensise and Pantosti, 2001; Galli and Peronace, 2015), so our samples represent erosion over at least one, and probably several, seismic cycles (Table 2).

Our results highlight the importance of transient erosional responses. Higher ^{10}Be erosion rates are found in catchments experiencing faster transient responses (i.e. faster knickpoint propagation), due to a combination of more effective fluvial incision, hillslope steepening, and enhanced landslide activity; and several of these processes seem to operate at similar rates (Figs. 4 and 5; e.g. Burbank et al., 1996; Larsen and Montgomery, 2012). Furthermore, the 2 to 6-fold downstream increase in erosion rates associated with the transient response (Fig. 5a) is comparable to the reported ~2 to 3-fold increase in base level lowering rates that triggered these responses (Olivetti et al., 2012; Roda-Boluda and Whittaker, 2017, 2018). Therefore, both spatial (i.e. along the faults, Fig. 3 and 4) and temporal (i.e. above and below knickpoints) variations in fault throw rates result in erosion-rate changes of similar magnitude to the throw rate differences.

5.2. Landsliding and ^{10}Be erosion rates

Landslides in the study area are not a perturbation from 'regular' erosional processes; instead they are an integral, and likely dominant part of the catchment transient erosional dynamics and sediment fluxes (Figs. 5 and 6). Despite landsliding being the main erosional process, which could affect CRN concentrations, we argue that in our study area ^{10}Be erosion rates accurately represent catchment-averaged, long-term erosion rates (Figs. 4a and 7). This is possible because: (1) landslides are generally ≤3 m deep, and the long-term landslide sediment fluxes are not volumetrically-dominated by the largest landslides (Section 2; see also supplementary material and Roda-Boluda et al., 2018); (2) they are frequent enough to create high landslide densities in the catchments (2–30%, Figs. 2 and 6b; above the 1% threshold for accuracy suggested by Yanites et al., 2009); this high frequency in time and space allows spatial and temporal variations in CRN concentrations to be adequately averaged; and (3) the erosional timescale of our ^{10}Be samples, of ~0.9 to 7 kyr (Table 2), compared to earthquake recurrence intervals in the area (see section 2), means that they represent a combination of co- and post-seismic landsliding, and landslide and non-landslide erosion between landslide-triggering events.

Our hypothesis that adequate sediment mixing can occur as landslides are progressively eroded from the hillslopes is supported by the accuracy tests of Fig. 7c, and by data from Li et al. (2016), who found that suspended sediment yield in catchments of the Longmen Shan are correlated with their earthquake-triggered landslide densities, and that for suspended sediment fractions, direct connectivity of the landslides with the fluvial network is not relevant because fine grain sizes are easily mobilised from hillslopes. Existing CRN-sediment mixing models (Niemi et al., 2005; Yanites et al., 2009) only account for fluvial mixing, and imply that CRN mixing is more effective as drainage area increases. Hence, large and small catchments should yield systematically different CRN concentrations, but field studies have found no evidence of this expected discrepancy (Scherler et al., 2014; Foster and Anderson, 2016), and sediment from large catchments is not al-

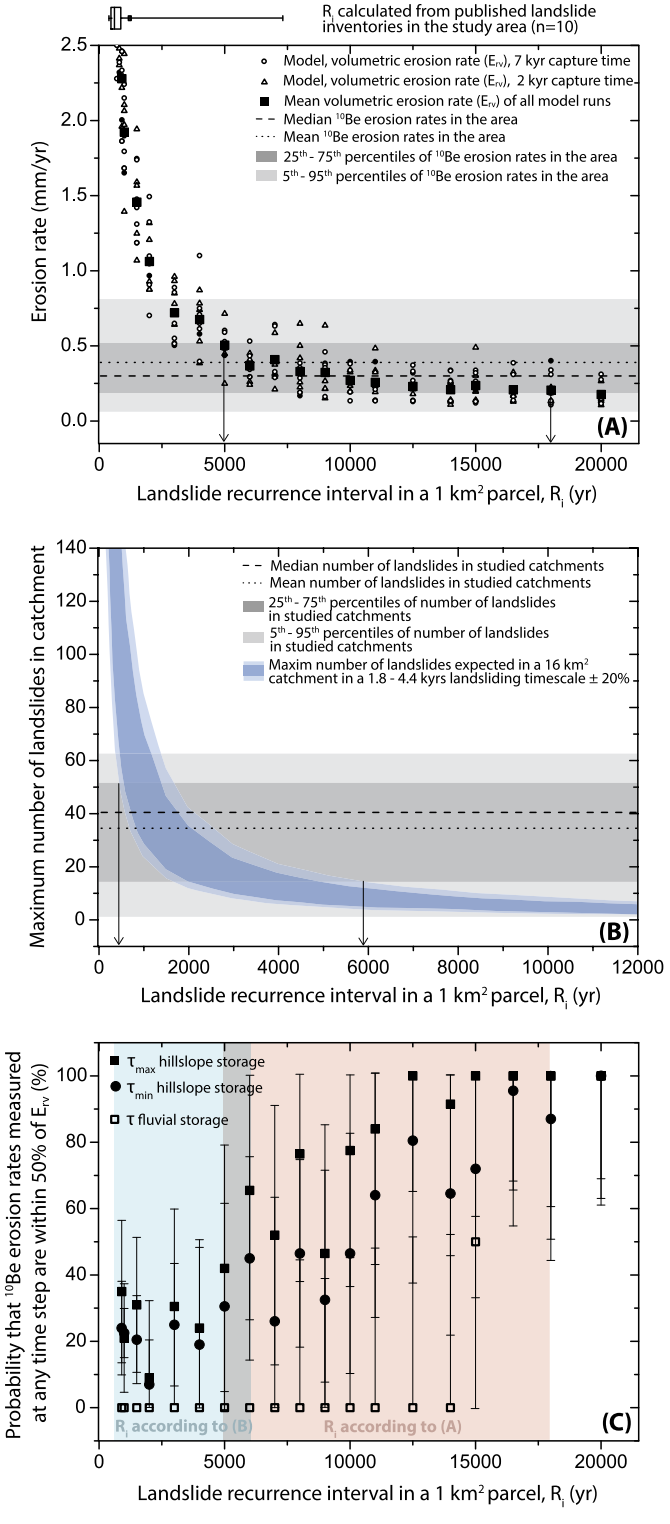

Fig. 7. Results of the application of Yanites et al. (2009) model for different plausible erosional and sediment mixing scenarios, for a hypothetical catchment with characteristics representative of our sampled catchments. (a) Long-term, volumetric erosion rates (E_{rv}) obtained from all model runs, for different landslide recurrence interval values (R_i). The "box plot" of all 30 ^{10}Be erosion rates obtained below knickpoints in the area (Fig. 1) is shown as a shaded box. The box plot on top of the *x*-axis shows the distribution of R_i values that can be inferred from 10 multi-temporal landslide inventories in the study area (see supplementary material). (b) Maximum number of landslides expected in a 16 km^2 catchment given the likely range of landsliding timescales (1.8–4.4 kyrs ±20% error; Fig. 6a), for different R_i values. The shaded "box plot" shows the range of numbers of landslides identified in the sampled catchments (Table 1). (c) Median values, for all model runs for each R_i, of the probability that samples measured at any given time step have a CRN concentration that would yield erosion rates within 50% of the long-term, volumetric erosion rates of Fig. 7a, E_{rv}. Results are shown for the mixing time, τ of the fluvial storage sediment mixing scenario, and for two potential end-members of hillslope storage τ_{max} and τ_{min}. Symbols show the median probability of samples' accuracies for the 12 model runs done for each R_i, with the total scatter between model runs shown as error bars. Results of these model runs can also be found as a table in the supplementary material.

ways adequately mixed (Kober et al., 2012; Puchol et al., 2014; West et al., 2014). Therefore, we suggest that hillslopes should be included as an important component of sediment mixing in future CRN sediment mixing models.

Moreover, our implementation of Yanites et al.'s (2009) model suggests that, provided that there is information about the likely accuracy of the ^{10}Be erosion rates and the size distribution and area-volume scaling of landslides (which can easily be extracted from geomorphological landslide inventories), first-order constraints can be placed on long-term landslide recurrence intervals, R_i, using CRN data (Fig. 7). Here, an R_i value of the order of ~6 kyrs/km^2 seems most plausible. Short-term (2–88 yrs), time-averaged R_i values can also be inferred from published multi-temporal landslide inventories of the study area (box plot in the upper x-axis in Fig. 7a; see supplementary material for a summary table and reference list). Most published inventories imply $R_i \ll 6$ kyrs/km^2, which, if representative of long-term landslide activity, would produce erosion rates and numbers of landslides considerably greater than observed (Fig. 7a and b). Although the disagreement regarding landslide numbers may partially be due to our geomorphological inventory under-estimating the frequency of landslides <0.04 km^2 (see Methods), the differences between erosion rates predicted if $R_i \ll 6$ kyrs/km^2, and those measured from ^{10}Be concentrations are harder to reconcile. This discrepancy could suggest that short-term inventories are not representative of long-term landsliding, that many landslides in these multi-temporal inventories are reactivations of older landslides, and/or that landslide frequency has increased in the past century with respect to long-term rates, potentially due to changing climate or human land-cover modifications (e.g. Remondo et al., 2005; Polemio and Petrucci, 2010). Therefore, our study shows that integrating landslide inventory and CRN data into numerical models could allow us to gain important insights about the evolution of landslide frequencies and erosion rates.

6. Conclusions

Our ^{10}Be data for southern Italy reveal catchment erosion rates of 0.10–0.64 mm/yr that are primarily controlled by fault throw rates and the extent of transient incision and landsliding, with spatial and temporal changes in fault throw rates resulting in erosion rate differences of similar magnitude and sensitivity. Those parts of the landscape that have not yet responded to active faulting erode consistently at ~0.1 mm/yr, while downstream of knickpoints, erosion is removing ~50% of the rock being uplifted by the faults. Landslides are an integral part of the transient erosional dynamics, and remarkably do not add significant noise to the large CRN data set of the study area. We suggest that this is due to landslides in the area being frequent, small and shallow; widespread within the catchments, and probably the result of several seismic cycles. The well-grounded accuracy of our ^{10}Be erosion rates allows us to constrain, using Yanites et al. (2009) numerical model, plausible landslide recurrence intervals and sediment mixing conditions, highlighting the potential of CRN data to study landslide dynamics.

Author contributions

DRB conceived the idea of investigation, planned the data collection, performed the data analyses, and prepared the figures, with feedback from MD and AW. Sample collection was carried out by DRB, MD and AW. Sample preparation and analyses were done by DRB with guidance from DG and AR. DRB wrote the manuscript with feedback from all authors.

Acknowledgements

DRB and MD were funded by the Janet Watson bursary scheme at the Department of Earth Science and Engineering of Imperial College London. Field campaigns were funded by the Geological Society of London Annie Greenly Fund, the British Society for Geomorphology Postgraduate Research Grant, and the British Sedimentological Research Group Gill Harwood Fund, awarded to DRB. CRN analyses were funded under the NERC CIAF Grant (project 9148/0414) awarded to DRB and AW. We thank Dylan Rood, Hugh Sinclair and Sanjeev Gupta for fruitful discussions; Sheng Xu for his help at the SUERC AMS Laboratory; and Jordan McDonald for assistance with field work. We thank an anonymous reviewer for thoughtful reviews that improved the manuscript.

Appendix A. Supplementary material

Supplementary material related to this article can be found online at https://doi.org/10.1016/j.epsl.2018.11.032.

References

Amato, A., Aucelli, P., Cinque, A., 2003. The long-term denudation rate in the Southern Apennines Chain (Italy): a GIS-aided estimation of the rock volumes eroded since middle Pleistocene time. Quat. Int. 101, 3–11.
Attal, M., Cowie, P., Whittaker, A., Hobley, D., Tucker, G., Roberts, G.P., 2011. Testing fluvial erosion models using the transient response of bedrock rivers to tectonic forcing in the Apennines, Italy. J. Geophys. Res., Earth Surf. 2003–2012, 116.
Balco, G., Stone, J.O., Lifton, N.A., Dunai, T.J., 2008. A complete and easily accessible means of calculating surface exposure ages or erosion rates from ^{10}Be ^{26}Al measurements. Quat. Geochronol. 3, 174–195.
Bierman, P., Steig, E.J., 1996. Estimating rates of denudation using cosmogenic isotope abundances in sediment. Earth Surf. Process. Landf. 21, 125–139.
Binnie, S.A., Phillips, W.M., Summerfield, M.A., Fifield, L.K., 2007. Tectonic uplift, threshold hillslopes, and denudation rates in a developing mountain range. Geology 35, 743–746.
Borchers, B., et al., 2016. Geological calibration of spallation production rates in the CRONUS-Earth Project. Quat. Geochronol. 31, 188–198.
Brown, E.T., Stallard, R.F., Larsen, M.C., Raisbeck, G.M., Yiou, F., 1995. Denudation rates determined from the accumulation of in situ-produced ^{10}Be in the Luquillo Experimental Forest, Puerto Rico. Earth Planet. Sci. Lett. 129 (1–4), 193–202.
Burbank, D.W., Leland, J., Fielding, E., Anderson, R.S., Brozovic, N., Reid, M.R., Duncan, C., 1996. Bedrock incision, rock uplift and threshold hillslopes in the northwestern Himalayas. Nature 379, 505–510.
Carretier, S., Regard, V., Vassallo, R., Aguilar, G., Martinod, J., Riquelme, R., Christophoul, F., Charrier, R., Gayer, E., Farías, M., 2015. Differences in ^{10}Be concentrations between river sand, gravel and pebbles along the western side of the central Andes. Quat. Geochronol. 27, 33–51.
Cowie, P., Attal, M., Tucker, G., Whittaker, A., Naylor, M., Ganas, A., Roberts, G., 2006. Investigating the surface process response to fault interaction and linkage using a numerical modelling approach. Basin Res. 18, 231–266.
Cowie, P.A., Roberts, G.P., 2001. Constraining slip rates and spacings for active normal faults. J. Struct. Geol. 23, 1901–1915.
Cyr, A.J., Granger, D.E., Olivetti, V., Molin, P., 2010. Quantifying rock uplift rates using channel steepness and cosmogenic nuclide-determined erosion rates: examples from northern and southern Italy. Lithosphere 2, 188–198.
Densmore, A.L., Ellis, M.A., Anderson, R.S., 1998. Landsliding and the evolution of normal fault-bounded mountains. J. Geophys. Res., Solid Earth 103, 15203–15219.
Densmore, A.L., Dawers, N.H., Gupta, S., Guidon, R., Goldin, T., 2004. Footwall topographic development during continental extension. J. Geophys. Res., Earth Surf. 109.
Densmore, A.L., Hetzel, R., Ivy-Ochs, S., Krugh, W.C., Dawers, N., Kubik, P., 2009. Spatial variations in catchment-averaged denudation rates from normal fault footwalls. Geology 37, 1139–1142.
DiBiase, R.A., Whipple, K.X., Heimsath, A.M., Ouimet, W.B., 2010. Landscape form and millennial erosion rates in the San Gabriel Mountains, CA. Earth Planet. Sci. Lett. 289, 134–144.
Dunai, T.J., 2010. Cosmogenic Nuclides: Principles, Concepts and Applications in the Earth Surface Sciences. Cambridge University Press.
Foster, M.A., Anderson, R.S., 2016. Assessing the effect of a major storm on ^{10}Be concentrations and inferred basin-averaged denudation rates. Quat. Geochronol. 34, 58–68.
Galli, P., Bosi, V., 2002. Paleoseismology along the Cittanova fault: implications for seismotectonics and earthquake recurrence in Calabria (southern Italy). J. Geophys. Res., Solid Earth 107 (B3). ETG 1-1–ETG 1-19.

Galli, P.A., Peronace, E., 2015. Low slip rates and multimillennial return times for Mw 7 earthquake faults in southern Calabria (Italy). Geophys. Res. Lett. 42, 5258–5265.
Gioia, D., Martino, C., Schiattarella, M., 2011. Long-to short-term denudation rates in the southern Apennines: geomorphological markers and chronological constraints. Geol. Carpath. 62, 27–41.
Kirby, E., Whipple, K.X., 2012. Expression of active tectonics in erosional landscapes. J. Struct. Geol.
Kober, F., Hippe, K., Salcher, B., Ivy-Ochs, S., Kubik, P., Wacker, L., Hählen, N., 2012. Debris-flow-dependent variation of cosmogenically derived catchment-wide denudation rates. Geology 40, 935–938.
Korup, O., Görüm, T., Hayakawa, Y., 2012. Without power? Landslide inventories in the face of climate change. Earth Surf. Process. Landf. 37 (1), 92–99.
Lal, D., 1991. Cosmic ray labeling of erosion surfaces: in situ nuclide production rates and erosion models. Earth Planet. Sci. Lett. 104, 424–439.
Larsen, I.J., Montgomery, D.R., Korup, O., 2010. Landslide erosion controlled by hillslope material. Nat. Geosci. 3 (4), 247–251.
Larsen, I.J., Montgomery, D.R., 2012. Landslide erosion coupled to tectonics and river incision. Nat. Geosci. 5, 468–473.
Lazzari, M., Schiattarella, M., 2010. Estimating long to short-term erosion rates of fluvial vs mass movement processes: an example from the axial zone of the southern Italian Apennines. Ital. J. Agron. 5, 57–66.
Li, G., West, A.J., Densmore, A.L., Hammond, D.E., Jin, Z., Zhang, F., Wang, J., Hilton, R.G., 2016. Connectivity of earthquake-triggered landslides with the fluvial network: implications for landslide sediment transport after the 2008 Wenchuan earthquake. J. Geophys. Res., Earth Surf. 121, 703–724.
Niemi, N.A., Oskin, M., Burbank, D.W., Heimsath, A.M., Gabet, E.J., 2005. Effects of bedrock landslides on cosmogenically determined erosion rates. Earth Planet. Sci. Lett. 237, 480–498.
Olive, J.A., Behn, M.D., Malatesta, L.C., 2014. Modes of extensional faulting controlled by surface processes. Geophys. Res. Lett. 41, 6725–6733.
Olivetti, V., Cyr, A.J., Molin, P., Faccenna, C., Granger, D.E., 2012. Uplift history of the Sila Massif, southern Italy, deciphered from cosmogenic ^{10}Be erosion rates and river longitudinal profile analysis. Tectonics 31.
Ouimet, W.B., Whipple, K.X., Granger, D.E., 2009. Beyond threshold hillslopes: channel adjustment to base-level fall in tectonically active mountain ranges. Geology 37, 579–582.
Ouimet, W.B., 2010. Landslides associated with the May 12, 2008 Wenchuan earthquake: implications for the erosion and tectonic evolution of the Longmen Shan. Tectonophysics 491, 244–252.
Patacca, E., Sartori, R., Scandone, P., 1990. Tyrrhenian basin and Apenninic arcs: kinematic relations since late Tortonian times. Mem. Soc. Geol. Ital. 45, 425–451.
Polemio, M., Petrucci, O., 2010. Occurrence of landslide events and the role of climate in the twentieth century in Calabria, southern Italy. Q. J. Eng. Geol. Hydrogeol. 43 (4), 403–415.
Puchol, N., Lavé, J., Lupker, M., Blard, P.-H., Gallo, F., France-Lanord, C., Team, A., 2014. Grain-size dependent concentration of cosmogenic ^{10}Be and erosion dynamics in a landslide-dominated Himalayan watershed. Geomorphology 224, 55–68.
Remondo, J., Soto, J., González-Díez, A., de Terán, J.R.D., Cendrero, A., 2005. Human impact on geomorphic processes and hazards in mountain areas in northern Spain. Geomorphology 66, 69–84.
Roda-Boluda, D.C., Whittaker, A.C., 2017. Structural and geomorphic constraints on active normal faulting and landscape evolution in Calabria, Italy. J. Geol. Soc. 174, 701–720.
Roda-Boluda, D.C., Whittaker, A.C., 2018. Normal fault evolution and coupled landscape response: examples from the Southern Apennines, Italy. Basin Res. 30, 186–209.
Roda-Boluda, D.C., D'Arcy, M., McDonald, J., Whittaker, A.C., 2018. Lithological controls on hillslope sediment supply: insights from landslide activity and grain size distributions. Earth Surf. Process. Landf. 43, 956–977.
Scherler, D., Bookhagen, B., Strecker, M.R., 2014. Tectonic control on ^{10}Be-derived erosion rates in the Garhwal Himalaya, India. J. Geophys. Res., Earth Surf. 119, 83–105.
Spina, V., Tondi, E., Mazzoli, S., 2011. Complex basin development in a wrench-dominated back-arc area: tectonic evolution of the Crati Basin, Calabria, Italy. J. Geodyn. 51, 90–109.
Stock, G.M., Frankel, K.L., Ehlers, T.A., Schaller, M., Briggs, S.M., Finkel, R.C., 2009. Spatial and temporal variations in denudation of the Wasatch Mountains, Utah, USA. Lithosphere 1, 34–40.
Stone, J., 2000. Air pressure and cosmogenic isotope production. J. Geophys. Res. 105, 23753–23759.
Strak, V., Dominguez, S., Petit, C., Meyer, B., Loget, N., 2011. Interaction between normal fault slip and erosion on relief evolution: insights from experimental modelling. Tectonophysics 513, 1–19.
Tofelde, S., Duesing, W., Schildgen, T.F., Wickert, A.D., Wittmann, H., Alonso, R.N., Strecker, M., 2018. Effects of deep-seated versus shallow hillslope processes on cosmogenic ^{10}Be concentrations in fluvial sand and gravel. Earth Surf. Process. Landf.
Trigila, A., Iadanza, C., Spizzichino, D., 2010. Quality assessment of the Italian Landslide Inventory using GIS processing. Landslides 7, 455–470.
Valensise, G., Pantosti, D., 2001. The investigation of potential earthquake sources in peninsular Italy: a review. J. Seismol. 5, 287–306.
West, A.J., Hetzel, R., Li, G., Jin, Z., Zhang, F., Hilton, R.G., Densmore, A.L., 2014. Dilution of ^{10}Be in detrital quartz by earthquake-induced landslides: implications for determining denudation rates and potential to provide insights into landslide sediment dynamics. Earth Planet. Sci. Lett. 396, 143–153.
Whipple, K.X., Tucker, G.E., 1999. Dynamics of the stream-power river incision model: implications for height limits of mountain ranges, landscape response timescales, and research needs. J. Geophys. Res., Solid Earth 1978–2012 (104), 17661–17674.
Whittaker, A.C., Attal, M., Cowie, P.A., Tucker, G.E., Roberts, G., 2008. Decoding temporal and spatial patterns of fault uplift using transient river long profiles. Geomorphology 100, 506–526.
Wobus, C., Whipple, K.X., Kirby, E., Snyder, N., Johnson, J., Spyropolou, K., Crosby, B., Sheehan, D., 2006. Tectonics from topography: procedures, promise, and pitfalls. Spec. Pap., Geol. Soc. Am. 398, 55.
Yanites, B.J., Tucker, G.E., Anderson, R.S., 2009. Numerical and analytical models of cosmogenic radionuclide dynamics in landslide-dominated drainage basins. J. Geophys. Res., Earth Surf. 114.